PNAS RESEARCH ARTICLE | ENGINEERING

Origami state machine with time-varying magnetic fields

Yifan Rao[a,1], Konstantinos Manos[b,1], Tuo Zhao[c], Minjie Chen[a,b,2], and Glaucio H. Paulino[c,d,2]

Affiliations are included on p. 10.

Edited by John A. Rogers, Northwestern University-Evanston, Evanston, IL; received April 29, 2026; accepted August 24, 2026

Achieving reliable, remote control over multiple stable states in modular systems remains a challenge due to the coupling between modules and history-dependent transitions. Here, we present magnetic origami state machines that enable deterministic navigation from any unknown initial state to any target state under magnetic actuation. By assuming mutually distinct energy barriers in modular Kresling origami assemblies, we realize fully accessible transition graphs with scalable state spaces. Guided by the graph associated to the state machine, a rotating magnetic field induces a universal reset that autonomously drives the system to a known equilibrium state from arbitrary states without sensing or feedback, while pulsed magnetic inputs further enable programmable transitions to any target state via prescribed actuation sequences. A reduced-order Lagrangian mechanics model predicts snap-through dynamics across reset, stepwise programming (between graph nodes), and shortcuts (by adapting pulse magnitude and orientation) where inertia triggers simultaneous multicell transitions with a single pulse. These results establish a general framework for programmable magneto-mechanical state machines with autonomous state reset and full state-space control.

origami dynamics | state machine | stability | multistability | magnetic actuation

Multistable structures provide a physical platform for functional reconfiguration and information storage, as discrete states can encode memory and logic without continuous energy input (1–9). Origami-inspired architectures are particularly promising as geometric folding enables compact assemblies with rich state spaces and programmable mechanical responses (10–17). An assembly of n bistable units admits up to 2^n stable configurations, yet scalable state spaces do not imply access to all states or controllable transitions between them (18–20). As the number of interacting units increases, state transitions become strongly coupled and history-dependent, precluding deterministic navigation through the full state space (21–24). Existing approaches that rely on contact-based mechanical loading limit applicability, particularly in scenarios such as untethered soft robots (25–29). While external stimuli such as magnetic actuation have enabled untethered control of origami assemblies (30–32), achieving deterministic navigation across the full state space under contactless actuation remains an open challenge. Another fundamental obstacle is that the current state of a multistable assembly may be unknown. Disturbances or incomplete actuation can drive the system into arbitrary configurations (33–35). Existing approaches, whether contact-based or contactless, implicitly assume a known starting state from which transition sequences are defined. This exposes a critical yet overlooked gap: without a known initial state, programmable transitions are impossible. The ability to autonomously initialize from any unknown configuration, without sensing, feedback, or prior state knowledge, is therefore a prerequisite for robust operation, yet remains to be demonstrated.

Here we present magnetic origami state machines that achieve complete state-space controllability within a unified contactless framework, enabling both deterministic navigation between arbitrary states and autonomous initialization from unknown configurations. Modular bistable Kresling assemblies with mutually distinct energy barriers admit fully accessible state-transition graphs, as illustrated by the representative four-cell example in Fig. 1 *A* and *B*. Guided by the graph associated with the state machine, a rotating magnetic field drives the system from arbitrary configurations to a unique chiral equilibrium without sensing, feedback, or prior state knowledge (Fig. 1*C*), thereby establishing a reference state. From this state, pulsed magnetic inputs traverse the graph to any target configuration via prescribed actuation sequences (Fig. 1*D*). A reduced-order Lagrangian model predicts the snap-through dynamics underlying reset, stepwise programming, and dynamics-enabled shortcuts, in which inertia enables simultaneous multicell transitions within a single magnetic pulse.

Significance

Multistable mechanical systems can encode information and functionality through transitions between discrete states. A key challenge consists of reliably programming such systems to a target state without prior knowledge of the current state. Here, we present origami-inspired multistable systems that can be initialized from unknown configurations and deterministically driven to target states under (global) magnetic actuation. A rotating magnetic field resets the system to a known state without sensing or feedback, whereas pulsed magnetic inputs enable transitions to desired configurations. This approach enables encrypted information storage, adaptive shape reconfiguration, and an untethered origami robot that navigates confined environments by changing its geometry. These findings pave the way to self-resetting mechanical systems without integrated electronics.

Author contributions: Y.R., K.M., T.Z., M.C., and G.H.P. designed research; Y.R. and K.M. performed research; Y.R., K.M, and T.Z. contributed new reagents/analytic tools; Y.R., K.M., T.Z., M.C., and G.H.P. analyzed data; and Y.R., K.M., T.Z., M.C., and G.H.P. wrote the paper.

The authors declare no competing interest.

This article is a PNAS Direct Submission.

Copyright © 2026 the Author(s). Published by PNAS. This article is distributed under Creative Commons Attribution-NonCommercial-NoDerivatives License 4.0 (CC BY-NC-ND).

[1]Y.R. and K.M. contributed equally to this work.

[2]To whom correspondence may be addressed. Email: minjie@princeton.edu or gpaulino@princeton.edu.

This article contains supporting information online at https://www.pnas.org/lookup/suppl/doi:10.1073/pnas.2615316123/-/DCSupplemental.

Published October 30, 2026.

Downloaded from https://www.pnas.org by PRINCETON UNIV LIBRARY; ACQUISITION SERVICE PERIODICALS on November 14, 2026 from IP address 140.180.240.0.

We demonstrate two applications enabled by the state-transition logic: information-oriented functionality via dual-key mechanical encoding, and embodied robotic functionality via an origami robot capable of on-demand reconfiguration for adaptive navigation in confined environments.

Results

Scalable State Space with Deterministic Transition Rules. We construct a four-cell Kresling origami assembly yielding $2^4 = 16$ discrete configurations (Fig. 1*A*) (*Origami State Machine Fabrication*). Each unit cell is bistable between a deployed (1) and a folded (0) state, with coupled axial displacement and twist rotation (18). All 16 configurations are mechanically stable under zero load (Fig. 2). To enable deterministic transitions between configurations, mutually distinct snap-through energy barriers ($\Delta U_y < \Delta U_r < \Delta U_w < \Delta U_b$) are programmed at the unit level (y ≡ yellow, r ≡ red, w ≡ white, b ≡ black) through geometric design and material selection (*Energy Barrier Characterization* and *SI Appendix*, sections S1 and S5). In the four-cell prototype (Fig. 1*A*), neighboring cells are assembled with an alternating chirality pattern (*LH–RH–LH–RH*). Left-handed (*LH*) cells fold under counterclockwise (ccw) torque, whereas right-handed (*RH*) cells fold under clockwise (cw) torque. A NdFeB permanent magnet with volume V and in-plane magnetization $\mathbf{m}$ is mounted on the top plate. Applying a uniform magnetic field $\mathbf{B}$ generates a ccw (L actuation) or cw (R actuation) magnetic torque $\boldsymbol{\tau}_{mag} = V\mathbf{m} \times \mathbf{B}$ that drives state transitions of the assembly (*Magnetic Actuation System* and *SI Appendix*, section S3).

Generalizing to an n-cell assembly, we define the chirality pattern $\mathbf{C} = (C_1, C_2, \ldots, C_n) \in \{+1, -1\}^n$, where $C_i = +1$ and $C_i = -1$ denote *LH* and *RH* cells, respectively, with cells indexed from bottom to top. The configuration is encoded by the state vector $\mathbf{S} = (S_1, S_2, \ldots, S_n) \in \{0, 1\}^n$, where $S_i = 0$ and $S_i = 1$ denote the folded and deployed states

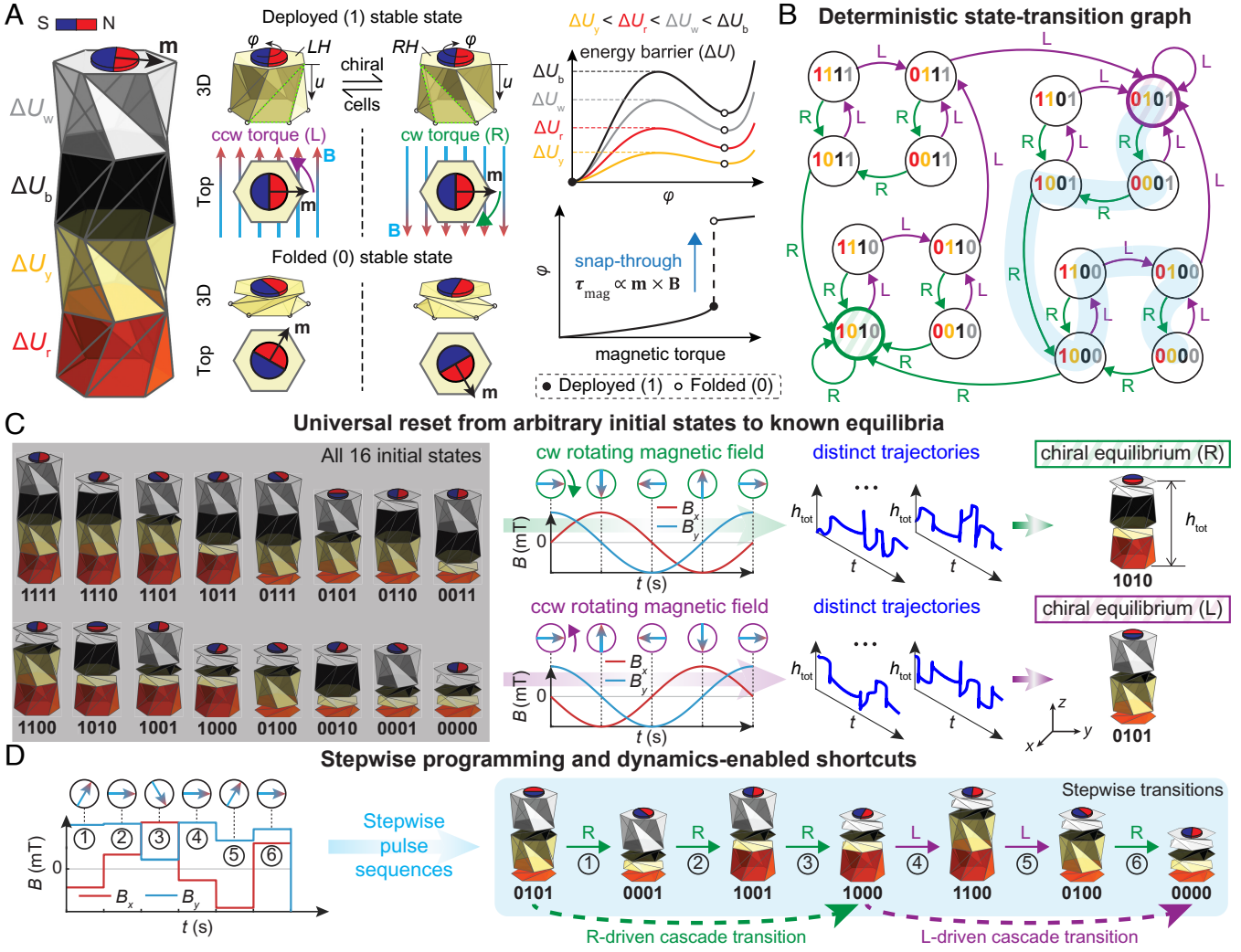


Fig. 1. Magnetic origami state machine. (*A*) System design and actuation mechanism. *Left*: Four-cell Kresling origami assembly with a top-mounted permanent magnet (in-plane magnetization **m**; red/blue: N/S poles). *Middle*: Each cell is bistable between deployed (1) and folded (0) states. Left-handed (*LH*) chiral cells fold under counterclockwise (ccw) torque (L actuation), whereas right-handed (*RH*) chiral cells fold under clockwise (cw) torque (R actuation). *Right*: schematic elastic energy landscapes of four cells with mutually distinct energy barriers $\Delta U_y < \Delta U_r < \Delta U_w < \Delta U_b$ (yellow < red < white < black). *Bottom*: single-cell twist angle vs. applied magnetic torque, illustrating the magnetic actuation mechanism. (*B*) Deterministic state-transition graph: 16 stable configurations (nodes) and 32 directed transitions (edges) under L (purple) and R (green) actuation. The two chiral equilibria 0101 and 1010 (highlighted by bold, shadowed circles) are unchanged under further L or R actuation. (*C*) Universal reset from arbitrary initial configurations to known equilibria. Under continuously rotating fields, any unknown initial state autonomously converges to a chiral equilibrium despite following distinct trajectories: ccw rotation to 0101 (L-equilibrium) and cw rotation to 1010 (R-equilibrium). (*D*) Stepwise programming and dynamics-enabled shortcuts. From the reset state 0101, the target state 0000 is reached either via six stepwise transitions or via a two-step cascade under prescribed magnetic pulses.

Downloaded from https://www.pnas.org by PRINCETON UNIV LIBRARY; ACQUISITION SERVICE PERIODICALS on November 14, 2026 from IP address 140.180.240.0.

of cell i, respectively. For an actuation step characterized by $\sigma = \mathrm{sgn}(\tau_{mag}) \in \{+1, -1\}$, with $\sigma = +1$ and $\sigma = -1$ denoting L and R actuation, respectively, the state-dependent chirality–actuation compatibility of cell i is defined as

$$\chi_i(\sigma, S_i) = \begin{cases} 1 & \text{if } S_i = 1 \text{ and } C_i\,\sigma = +1, \\ 1 & \text{if } S_i = 0 \text{ and } C_i\,\sigma = -1, \\ 0 & \text{otherwise.} \end{cases} \quad [1]$$

A cell can change its state only if it satisfies the compatibility condition, defining the active set $\mathcal{A}(\sigma, \mathbf{S}) = \{i : \chi_i(\sigma, S_i) = 1\}$. Within $\mathcal{A}$, the cell with the lowest energy barrier reaches the snap-through instability first and changes its state:

$$i^* = \underset{i \in \mathcal{A}(\sigma, \mathbf{S})}{\arg\min}\ \Delta U_i, \qquad S_{i^*} \mapsto 1 - S_{i^*}. \quad [2]$$

Assuming distinct energy barriers ($\Delta U_i \neq \Delta U_j$ for $i \neq j$), Eq. **2** yields a unique i^* when $\mathcal{A} \neq \emptyset$, whereas the assembly remains unchanged when $\mathcal{A} = \emptyset$. Together, these rules define the deterministic transition map $\mathbf{S}' = \mathcal{T}(\mathbf{S}, \sigma)$.

Based on the formulation above, assuming mutually distinct energy barriers, the following reachability theorem holds: for an arbitrary n-cell assembly with an arbitrary chirality pattern $\mathbf{C}$, any target state is reachable from any initial state through a finite sequence of binary actuation inputs (proved in *SI Appendix*, section S2).

Enumerating $\mathcal{T}(\mathbf{S}, \sigma)$ over all 2^n configurations and both actuation directions yields the deterministic state-transition graph $\mathcal{G} = (\mathcal{V}, \mathcal{E})$ with $|\mathcal{V}| = 2^n$ nodes and $|\mathcal{E}| = 2^{n+1}$ directed edges (see Fig. 1*B* for $n = 4$). The graph illustrates the proven reachability and identifies the equilibrium configurations. A configuration is an equilibrium under σ when $\mathcal{A} = \emptyset$, so that $\mathcal{T}(\mathbf{S}, \sigma) = \mathbf{S}$ (a self-loop in $\mathcal{G}$; Fig. 1*B*). From Eq. **1**, cell i is incompatible with σ when $S_i = (1 - C_i\sigma)/2$, which uniquely specifies the state of every cell in the equilibrium configuration. Hence each actuation direction admits a unique equilibrium, $\mathbf{S}^{eq}(\sigma) = (\mathbf{1} - \mathbf{C}\sigma)/2$, and the two equilibria $\mathbf{S}_L^{eq} = \mathbf{S}^{eq}(+1)$ and $\mathbf{S}_R^{eq} = \mathbf{S}^{eq}(-1)$ are bitwise complementary.

Full-State Navigation Via Pulsed Magnetic Fields. Executing the transitions prescribed by $\mathcal{G}$ in Fig. 1*B* requires mapping each configuration to the field orientation β that produces the desired actuation direction (L or R). Because the permanent magnet follows the twist of the assembly, each configuration `ijkl` corresponds to a unique in-plane magnetization angle φ_{ijkl}, measured to agree with geometric predictions within ±5° across all 16 configurations (Fig. 2*A*) (*Imaging-Based Transition Tracking* and *SI Appendix*, section S3). Directional actuation is achieved via uniform magnetic pulses once the generated torque exceeds the single-cell threshold. The angular offset $\delta = \beta - \varphi_{ijkl}$ sets the transition direction: $\delta > 0$ induces L actuation, while $\delta < 0$ induces R actuation (Fig. 2*B*). Using a constant field magnitude $B_0 = 42$ mT, a pulse duration of 3 s, and $\delta = \pm 73°$, we experimentally realize all stepwise transitions in $\mathcal{G}$ (Fig. 2*B*) via continuous sequential pulses T1–T48 (Fig. 2*C*). These results demonstrate fully contactless, deterministic access to the entire state space (Movie S1).

Reset from Arbitrary States Via Rotating Magnetic Fields. Deterministic transitions alone do not enable programmable operation when the current state is unknown. A reset mechanism is therefore required, and its existence is guaranteed by the convergence structure of $\mathcal{G}$. Under sustained actuation at fixed σ, repeated application of $\mathcal{T}(\cdot, \sigma)$ drives any initial configuration to the direction-dependent equilibrium. To see this, define the potential as

$$\Phi(\mathbf{S}, \sigma) = \sum_{i:\, C_i\,\sigma = +1} S_i \;+ \sum_{i:\, C_i\,\sigma = -1} (1 - S_i), \quad [3]$$

which counts the number of cells eligible for transition under σ. Each application of $\mathcal{T}$ reduces Φ by exactly one, so the process terminates in at most n steps at the unique equilibrium $\mathbf{S}^{eq}(\sigma)$. Thus, for the four-cell example shown in Fig. 1, any initial configuration converges to the L-equilibrium $\mathbf{S}_L^{eq} = \mathtt{0101}$ under sustained L actuation and to R-equilibrium $\mathbf{S}_R^{eq} = \mathtt{1010}$ under sustained R actuation, in at most four steps. For example, from `0111`, $\Phi(\mathtt{0111}, +1) = 1$ and $\Phi(\mathtt{0111}, -1) = 3$, implying one L actuation step to `0101` but three R steps to `1010`.

Rotating magnetic fields provide a practical realization of this reset (Fig. 1*C*). As the field rotates, the instantaneous torque drives cyclic state transitions (Fig. 3*A* and Movie S2). Notably, multiple cells may undergo simultaneous state transitions. For example, the transition from `1010` to `0100` in Fig. 3*A* highlights the role of dynamical effects, including inertia and damping, in magnetic actuation. These effects are analyzed below using a self-developed Lagrangian framework. Nevertheless, convergence to $\mathbf{S}^{eq}$ is guaranteed by its absorbing nature: every nonequilibrium configuration satisfies $\mathcal{A} \neq \emptyset$ and therefore responds to the rotating field, whereas the equilibrium satisfies $\mathcal{A}(\sigma, \mathbf{S}^{eq}) = \emptyset$ and remains mechanically locked. The equilibrium thus persists over a disproportionately large angular interval per rotation cycle, defining a finite equilibrium retention window (Fig. 3*A*); terminating the field within this window leaves the system at $\mathbf{S}^{eq}$ regardless of initial state or transient pathway.

Experiments confirm universal convergence across all 16 initial configurations using ccw and cw rotating fields with magnitude $B_0 = 42$ mT and frequency $f = 0.1$ Hz (Fig. 3*B* and Movie S3). Under cw rotation, all trajectories converge to `1010`; under ccw rotation, all converge to `0101`. Since $\Phi \leq n = 4$ for any initial state, all transitions to equilibrium are complete within one full rotation. The field is therefore terminated after one complete cycle at $\varphi_{\mathtt{0101}} + 73°$ for ccw reset or $\varphi_{\mathtt{1010}} - 73°$ for cw reset, reliably placing the system within the retention window of the target equilibrium (Fig. 3*B*).

Stepwise Programming and Dynamics-Enabled Shortcuts. Following a reset to a known equilibrium, the system can be deterministically programmed to any target state by sequential magnetic pulses. Each magnetic pulse delivers a single L or R actuation, advancing the equilibrium system by one step along $\mathcal{G}$ via

$$\mathbf{S}^{(k)} = \mathcal{T}\big(\cdots \mathcal{T}\big(\mathcal{T}(\mathbf{S}^{eq}, \sigma_1), \sigma_2\big) \cdots, \sigma_k\big) = \mathbf{S}^{target}. \quad [4]$$

The minimum number of steps k^* from $\mathbf{S}^{eq}$ to $\mathbf{S}^{target}$ is the shortest-path distance in $\mathcal{G}$, obtained by breadth-first search (*SI Appendix*, section S2 and Table S2). Since the two equilibria generally yield different shortest-path distances to a given target, the choice of reset direction itself becomes part of the optimization. For instance, targeting `0000` from `0101` requires $k^* = 6$ steps (R–R–R–L–L–R), whereas from `1010` it requires $k^* = 10$ steps (L–L–L–L–R–R–R–L–L–R); ccw reset to `0101` is therefore preferred, and the six-step programming sequence is experimentally demonstrated in Fig. 3*C* and Movie S4. In

Downloaded from https://www.pnas.org by PRINCETON UNIV LIBRARY; ACQUISITION SERVICE PERIODICALS on November 14, 2026 from IP address 140.180.240.0.

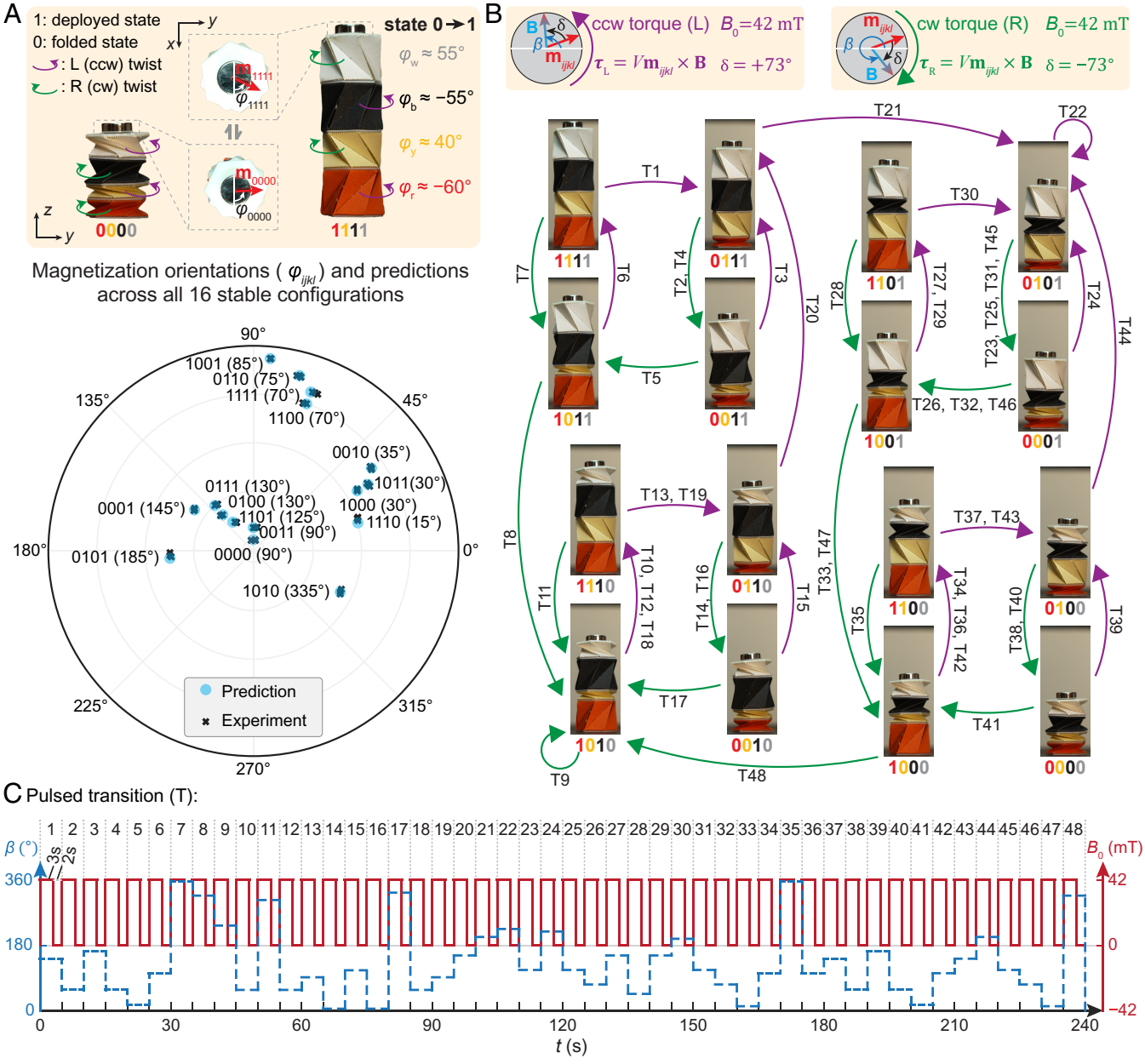


Fig. 2. Deterministic full-state navigation via pulsed magnetic fields. (*A*) Measured and predicted in-plane magnetization orientations φ_{ijkl} for all 16 stable configurations, showing agreement within ±5°. These state-dependent orientations define the mapping between applied field direction and the induced magnetic torque direction. (*B*) Pulse-driven navigation of the state-transition graph (Fig. 1*B*) using 48 sequential transitions (T1–T48). These transitions traverse all 32 unique directed edges, with selected edges repeated to enable continuous evolution across the full state space. (*C*) Magnetic field pulse sequences (magnitude B_0 and orientation β) used to execute the transitions in (*B*). For transition T22, a reduced offset angle of $\delta = +40°$ is used instead of $\delta = +73°$ to avoid overstretching near the L-equilibrium configuration.

addition, when both $\mathbf{S}^{initial}$ and $\mathbf{S}^{target}$ are known, the reset step can be bypassed entirely. The system is navigated directly from $\mathbf{S}^{initial}$ to $\mathbf{S}^{target}$ along the shortest path in $\mathcal{G}$, with the minimum number of steps given by

$$k^*_{direct} = d\left(\mathbf{S}^{initial}, \mathbf{S}^{target}\right), \quad [5]$$

read directly from the precomputed $2^n \times 2^n$ distance matrix D (*SI Appendix*, section S2 and Table S3). For example, navigating directly from 1100 to 0110 requires a minimum of $k^*_{direct} = 4$ steps (R–R–L–L).

Inspired by the simultaneous multicell transitions observed during rotating-field reset (Fig. 3*A*), we design a two-step pulsed actuation sequence to harness cascade dynamics as a shortcut (Fig. 3*D*). Magnetic pulse 1 drives 0101 → 1000 and magnetic pulse 2 drives 1000 → 0000, completing in two steps a transition that requires six steps along the quasi-static shortest path (Movie S4). Transient snapshots within each step reveal the cascade mechanism: intermediate configurations appear as fleeting transient states rather than stable stopping points, confirming that dynamical effects carry the system across multiple energy barriers in a single actuation.

Lagrangian Model of Snap-Through Dynamics. The simultaneous multicell transitions observed during reset and pulsed actuation motivate a reduced-order Lagrangian model to predict

Downloaded from https://www.pnas.org by PRINCETON UNIV LIBRARY; ACQUISITION SERVICE PERIODICALS on November 14, 2026 from IP address 140.180.240.0.

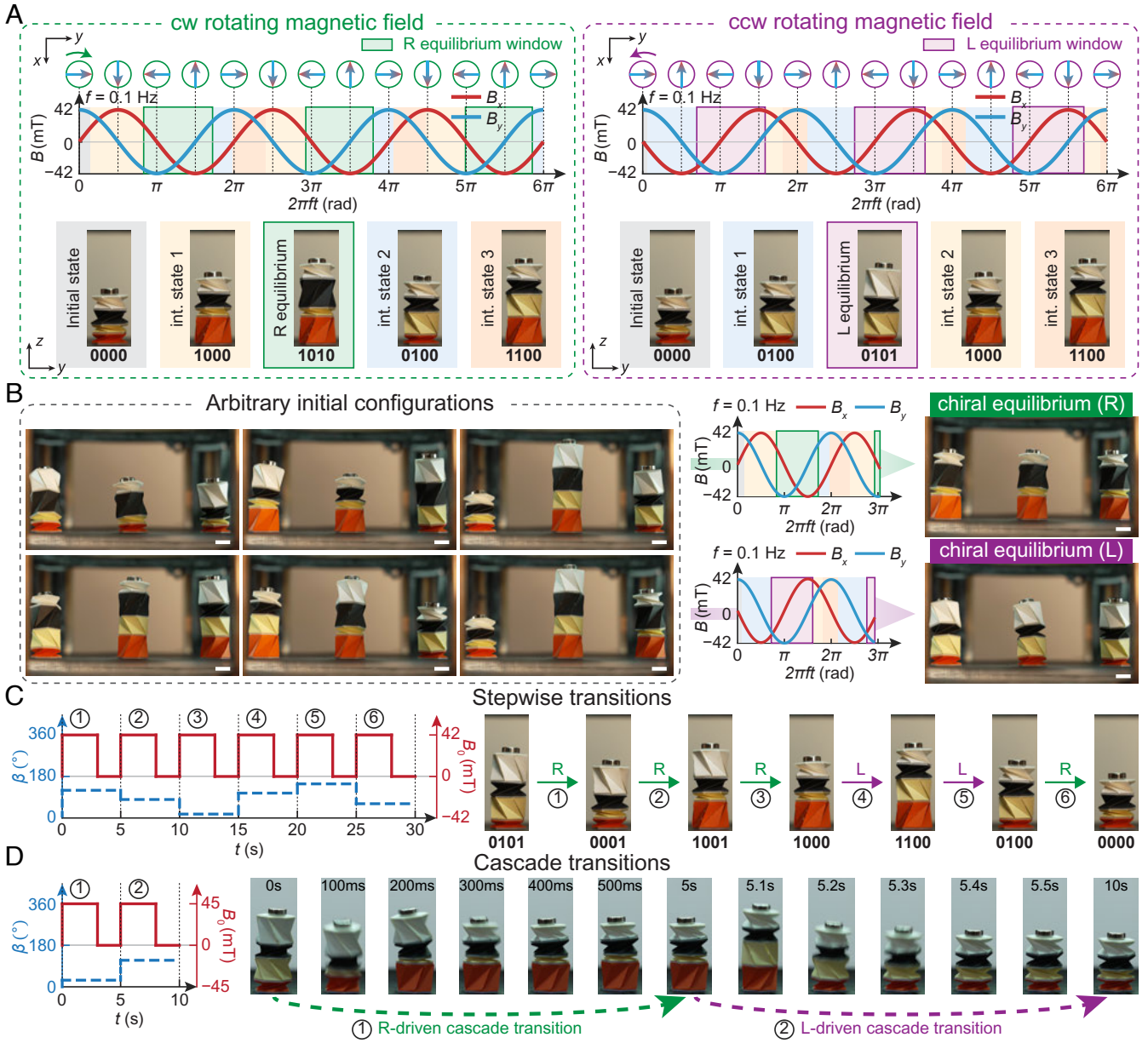


Fig. 3. Universal reset from arbitrary states via rotating magnetic fields and subsequent pulse–driven state programming. (*A*) Cyclic configuration switching and equilibrium retention under continuous field rotation ($B_0 = 42$ mT, $f = 0.1$ Hz), starting from configuration 0000. cw rotation drives the state machine through a repeating sequence of configurations, with the R-equilibrium (1010) retained over a disproportionately long angular (time) interval per cycle; ccw rotation yields analogous behavior converging to the L-equilibrium (0101). Green and purple bands mark the experimentally measured equilibrium windows, the angular ranges per rotation cycle over which each equilibrium is retained, whose finite width enables reliable field termination without precise timing. (*B*) Universal convergence from all 16 initial configurations under cw (*Top*) and ccw (*Bottom*) rotating fields. Despite variability in transient pathways, including cascade transitions involving simultaneous switching of multiple cells, all trajectories converge to the corresponding chiral equilibrium when the field is terminated within the equilibrium window. (*C*) From the L-equilibrium (0101), the target state 0000 is reached via stepwise transitions using a prescribed six-step pulse sequence (shortest path in the state-transition graph). (*D*) From the L-equilibrium (0101), the target state 0000 is instead reached via a prescribed two-step pulsed actuation shortcut; transient snapshots reveal cascade transitions. (Scale bar, 1 cm.).

cascade onset, actuation boundaries, and equilibrium retention windows. Each cell is described by axial displacement u_i and twist angle φ_i, with bistable energy landscapes calibrated from quasi-static tests (Fig. 4*A*). Applying the Euler–Lagrange equations yields

$$\begin{cases} m_i^{eff}(\ddot{u}_i + \nu\dot{u}_i) = F_{mech}^{(i+1)} - F_{mech}^{(i)}, \\ J_i^{eff}(\ddot{\varphi}_i + \nu\dot{\varphi}_i) = T_{mech}^{(i+1)} - T_{mech}^{(i)} + \tau_{mag}^{(i)}, \end{cases} \quad [6]$$

where m_i^{eff} and J_i^{eff} are the effective mass and moment of inertia of cell i, ν is a phenomenological viscous damping factor (36), and $F_{mech}^{(i)}$ and $T_{mech}^{(i)}$ denote the axial force and torque transmitted across the interface between cells $i-1$ and i with free-end boundary conditions $F_{mech}^{(n+1)} = T_{mech}^{(n+1)} = 0$. Magnetic actuation enters only at the top cell, with $\tau_{mag}^{(i)} = 0$ for $i < n$, while for $i = n$,

$$\tau_{mag}^{(n)}(t) = VM_0B_0\sin(\beta_0 + 2\pi ft - \alpha - \varphi_n), \quad [7]$$

where V and M_0 are the magnet volume and magnetization magnitude, B_0 is the applied field amplitude, α and β_0 are the initial orientations of the magnetization and the applied field, φ_n

Downloaded from https://www.pnas.org by PRINCETON UNIV LIBRARY; ACQUISITION SERVICE PERIODICALS on November 14, 2026 from IP address 140.180.240.0.

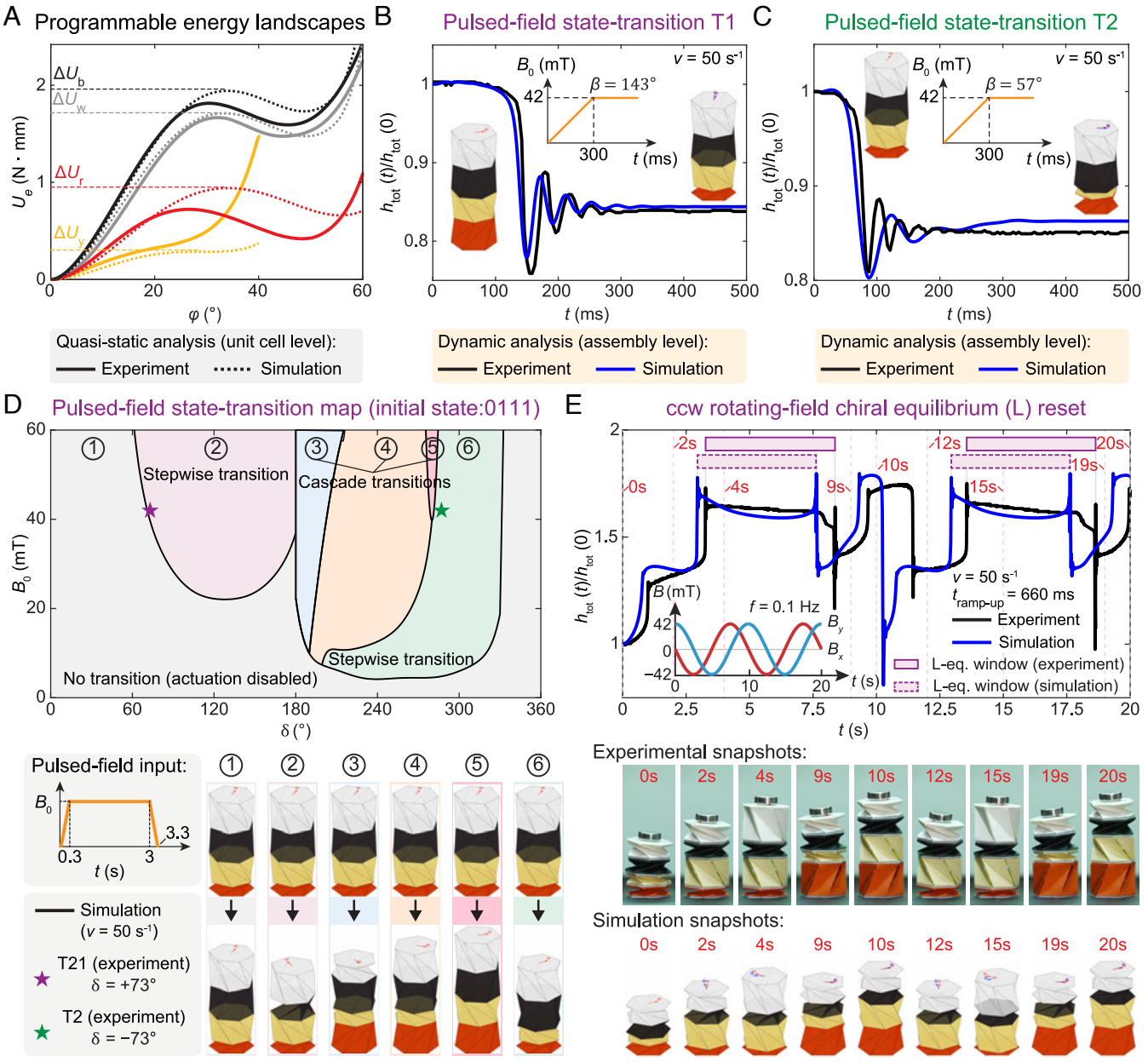


Fig. 4. Snap-through dynamics across reset, stepwise programming, and dynamics-enabled shortcuts. (*A*) Elastic energy landscapes $U_e(\varphi)$ for four cells, yielding mutually distinct barriers $\Delta U_y < \Delta U_r < \Delta U_w < \Delta U_b$. (*B* and *C*) Normalized height trajectories $h_{tot}(t)/h_{tot}(0)$ for pulsed transitions T1 (1111→0111) and T2 (0111→0011), showing agreement between experiment and simulation. The RMS errors (RMSEs) between the normalized experimental and simulated trajectories are 2.03% and 2.52%, respectively. (*D*) Simulated transition map from 0111 as a function of B_0 and δ: ① no transition; ②, ⑥ stepwise transitions; ③–⑤ cascade transitions. Stars mark experimental results for transitions T21 and T2 in Fig. 2. (*E*) Trajectories under ccw rotating field ($B_0 = 42$ mT, $f = 0.1$ Hz), showing agreement between experiment and simulation and a finite equilibrium retention (L-eq.) window.

is the twist angle of the magnet, and f is the actuation frequency, unifying pulsed ($f = 0$) and rotating-field ($f \neq 0$) actuation within a single framework. The chain structure of Eq. **6** explains cascade transitions: although τ_{mag} acts only on cell n, axial–torsional coupling distributes loading across the assembly, and a cascade occurs when multiple cells simultaneously exceed their snap-through barriers.

The model is validated against pulse-driven transitions, reproducing experimental height trajectories including timing, amplitude, and postsnap oscillations (Fig. 4 *B* and *C* and Movie S5). Sweeping over (B_0, δ) for configuration 0111 yields the phase diagram in Fig. 4*D*, delineating regimes of no transition, stepwise transitions, and cascade transitions, and identifying a dynamically safe operating window bounded by cascade onset and stepwise transition failure. The experimental parameters ($B_0 = 42$ mT, $\delta = \pm 73°$) lie within this predicted window. Applied to rotating fields, the model quantitatively predicts both transient transition sequences and the finite equilibrium retention window observed experimentally (Fig. 4*E* and Movie S5). Simulations across all 16 initial configurations further reveal distinct trajectories under identical actuation that nevertheless converge within overlapping retention windows (Fig. 5). These trajectories exhibit cyclic divergence and convergence, collapsing to a common equilibrium within the retention window while diverging and reconverging across cycles. This process establishes a one-to-one mapping between

Downloaded from https://www.pnas.org by PRINCETON UNIV LIBRARY; ACQUISITION SERVICE PERIODICALS on November 14, 2026 from IP address 140.180.240.0.

transient response and initial state, providing a basis for robust resetting.

Together, the Lagrangian framework elevates protocol design from empirical tuning to mechanics-based prediction. This predictive capability further enables model-guided design of actuation strategies in larger systems, as demonstrated, for example, for a five-cell origami state machine in *SI Appendix*, section S6. Details of the model and experimental measurements are provided in *Imaging-Based Transition Tracking* and *Reduced-Order Dynamics Modeling* and *SI Appendix*, sections 1 and 3–5.

Applications.

Dual-key mechanical encryption. The rotating-field reset exhibits a fundamental duality: identical actuation yields identical final equilibria across all initial configurations, erasing information from any static observation, while distinct transient trajectories (Fig. 5) encode each initial state as a dynamic fingerprint accessible only via local measurement. These complementary properties enable a dual-key encryption protocol (Fig. 6). A sender (Alice) encodes a message symbol into one of the 16 stable configurations. A universal ccw rotating-field reset drives the system to the L-equilibrium 0101 while simultaneously generating a configuration-dependent transient response that encodes the initial state as a dynamic fingerprint. A subsequent deterministic pulse sequence maps the system to a publicly observable configuration 0000. An authorized receiver (Bob), possessing both the actuation protocol (Key 1) and a reference library of transient fingerprints (Key 2), recovers the payload by matching the observed transient response to the corresponding configuration. An interceptor (Mallory), with access only to Key 1, observes an identical postreset equilibrium regardless of the encoded message, as all initial configurations converge to the same

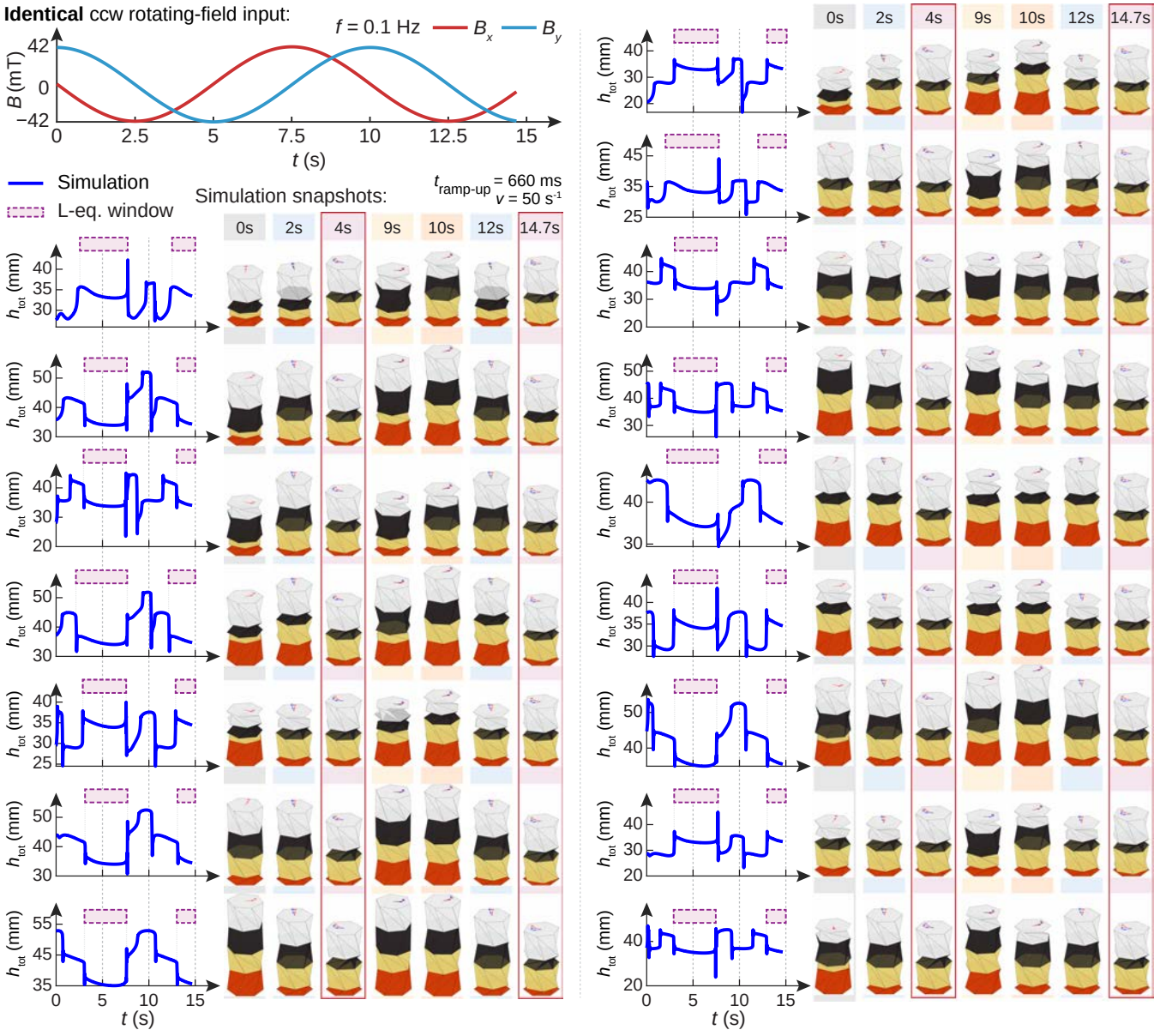


Fig. 5. Transient dynamics fingerprint initial configurations while ensuring robust convergence to equilibrium. Simulated height trajectories $h_{tot}(t)$ for all 16 initial configurations under the same ccw rotating field (*Top Left*) differ markedly despite identical actuation. Trajectories exhibit cyclic divergence and convergence: they collapse to the same equilibrium within the retention window, diverge in the subsequent cycle, and reconverge upon reentry, as highlighted by the red snapshots. These observations establish a one-to-one mapping between transient response and initial state. Overlapping equilibrium retention windows (purple dashed boxes) define a common field-termination interval, enabling a reliable reset independent of the initial configuration. L-eq., L-equilibrium.

Downloaded from https://www.pnas.org by PRINCETON UNIV LIBRARY; ACQUISITION SERVICE PERIODICALS on November 14, 2026 from IP address 140.180.240.0.

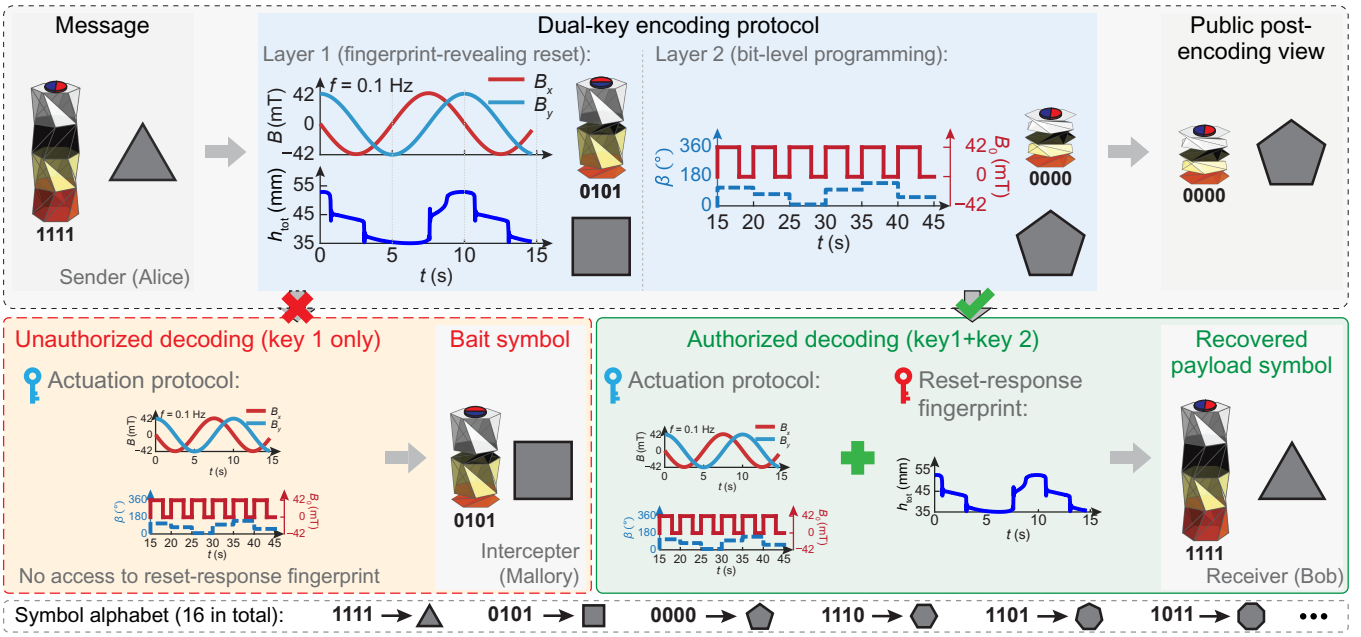


Fig. 6. Dual-key physical encoding enabled by transient–equilibrium separation. A symbolic message encoded in the origami state machine is protected by a two-layer protocol. Key 1 (actuation protocol): prescribed magnetic inputs comprising both a universal rotating-field reset and subsequent programming pulses, which drive the system to a public postencoding configuration. Key 2 (transient fingerprint): the locally recorded reset response that encodes the initial configuration. Authorized decoding requires both keys to recover the encoded symbol. In contrast, access to the actuation protocol alone yields indistinguishable equilibrium states and leads to incorrect decoding. The symbol alphabet comprises 16 distinct configurations, demonstrating protocol-level control over access to mechanically encoded information.

state; the encoded information is thus unrecoverable from the final state alone. This protocol demonstrates that the nonlinear dynamics of the origami state machine enable intrinsic, physics-based access control over mechanically encoded information

StateMorph: Adaptive origami robot. The state-transition logic can also be mapped to embodied robotic functions. *StateMorph* embeds the origami state machine within a locomoting body, enabling deterministic access to multiple configurations under uniform magnetic fields (*StateMorph Robot Design and Fabrication*). A rotating field drives rolling locomotion, while bilinear ramp pulses execute selective cell switching according to the state-transition rules, thereby unifying locomotion and reconfiguration within a single contactless actuation framework (Fig. 7 and Movie S6).

Rolling and transition modes are enabled by magnetic and frictional asymmetries. First, permanent magnets embedded in the end caps, with magnetization vectors $\mathbf{m}_{red}$ and $\mathbf{m}_{white}$ offset by $\Delta\varphi$, partition the field-orientation space into rolling regions and transition regions (Fig. 7*A*). In the rolling regions, the combined torque produces a net moment that exceeds the frictional threshold, driving whole-body locomotion (Fig. 7 *B* and *C*). In the switching regions, the torques are almost opposing, yielding a net moment insufficient to overcome the frictional threshold for rigid motion, while still generating sufficient internal axial–torsional loading to exceed the snap-through barrier of the target cell (Fig. 7 *B* and *C*). Second, asymmetric end-cap edge thicknesses produce differential friction coefficients (μ_{high} and μ_{low}), ensuring that during a switching pulse the high-friction end anchors the robot against residual motion while the low-friction end displaces, localizing snap-through to the target cell (Fig. 7*A*).

In a representative demonstration, the robot navigates a stepped channel whose narrow central section is approximately 20% smaller than the open sections, blocking the deployed assembly but permitting passage in folded states (Fig. 7*D*). Starting from the fully deployed state 1111, the robot rolls forward under a rotating field until contact with the channel wall arrests locomotion (phase I). Two successive switching pulses fold the two upper cells (1111→0111→0011), reducing the cross-sectional profile and enabling traversal of the constriction (phases II–III), after which rolling resumes (phase IV). Upon reaching open space, a redeployment pulse restores one folded cell (0011→1011, phase V), and the robot reverses direction under continued actuation until blocked again (phase VI). A final folding pulse (1011→1010) reduces the profile for return passage (phase VII), followed by exit from the channel (phase VIII) (Movie S6). Throughout all phases, actuation is achieved solely through a globally uniform magnetic field, without sensing, feedback, or tethering.

Discussion

We demonstrate a Kresling origami state machine that achieves full state-space accessibility under global, contactless magnetic actuation. Guided by its state-transition graph, a rotating magnetic field enables universal reset from arbitrary configurations, whereas pulsed magnetic fields with varying magnitude and orientation enable both deterministic stepwise programming to any target state and inertia-driven cascade transitions that provide dynamics-enabled shortcuts by compressing multistep pathways.

A reachability theorem establishes that, under the assumption of mutually distinct energy barriers, any target state is reachable from any initial state through a finite actuation sequence for an arbitrary number of cells and any chirality pattern. The corresponding state-transition graph provides a complete representation of these accessible transitions. The reduced-order Lagrangian model predicts both the stepwise and cascade transitions under pulsed magnetic fields, as well as the rotating-field

Downloaded from https://www.pnas.org by PRINCETON UNIV LIBRARY; ACQUISITION SERVICE PERIODICALS on November 14, 2026 from IP address 140.180.240.0.

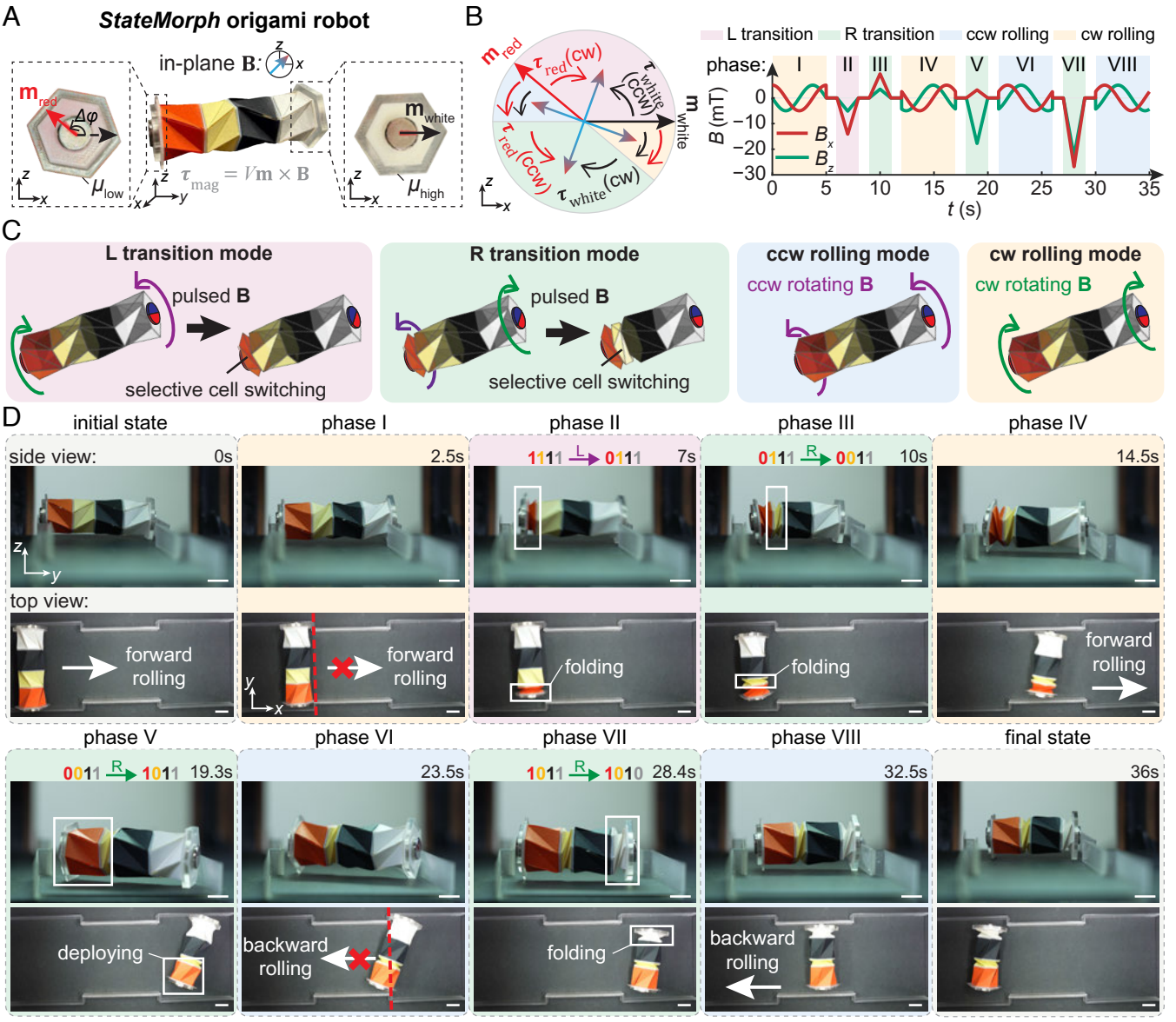


Fig. 7. *StateMorph*: An origami state machine-enabled robot with adaptive locomotion. (*A*) Robot design. Two permanent magnets embedded at opposite ends, with magnetization vectors $\mathbf{m}_{red}$ and $\mathbf{m}_{white}$ offset by $\Delta\varphi$, generate different magnetic torques (τ_{mag}) under a global, uniform in-plane field. Asymmetric terminal thickness yields differential friction coefficients (μ_{low}, μ_{high}) with the ground, enabling selective cell switching. (*B*) Actuation mechanism. *Left*: $\mathbf{m}_{red}$ and $\mathbf{m}_{white}$ partition the field-orientation space into four regions. ccw (blue) and cw (yellow) regions generate codirectional torques for rolling, whereas L transition (purple) and R transition (green) regions generate opposing torques to drive cell switching, as schematically illustrated in (*C*). Rolling is driven by a continuously rotating field, while switching is induced by bilinear ramp pulses. *Right*: A predefined field sequence programs eight phases of robot behavior (I–VIII), enabling adaptive locomotion. (*D*) Adaptive locomotion in constrained environments (side and top views). The robot rolls forward (phase I) until encountering a constraint, then undergoes sequential state transitions that reduce its cross-section (phase II: 1111→0111; phase III: 0111→0011), enabling passage through a narrow channel, followed by resumed rolling (phase IV). In open space, the folded cell is redeployed (phase V: 0011→1011), after which backward rolling (phase VI) is initiated until blocked. A further folding pulse (phase VII: 1011→1010) reduces the profile again, enabling return through the narrow channel (phase VIII). The on-demand locomotion or selective cell switching enables adaptive functionality under a global, untethered actuation framework. (Scale bar, 1 cm.).

reset, enabling model-guided design of magnetic actuation for deterministic programming in origami assemblies.

The programmable state-transition logic enables two complementary applications. For information-oriented functionality, the dual-key mechanical encoding protocol provides a mechanical analogue of challenge–response authentication (37), with reconfigurable transient fingerprints, nonvolatile information storage, and potential robustness in electromagnetically harsh environments. Conceptually, the same state-transition logic can be translated into embodied robotic functions, as demonstrated by the *StateMorph* robot, where deterministic state transitions produce adaptive morphological reconfiguration and locomotion under uniform magnetic fields. Together, these examples illustrate how a common state-transition framework supports both information-oriented and embodied robotic functionalities.

In summary, this work establishes a general framework for programmable multistable systems based on deterministic state-transition graphs and dynamics-guided state selection. The Kresling assembly and magnetic actuation provide experimental realization of this framework. Implementation-specific considerations, including addressability, operation of multiple origami state machines, and environmental effects, are discussed in *SI Appendix*, section S3D. Theoretically, the underlying reachability and state-transition principles are independent of the specific

Downloaded from https://www.pnas.org by PRINCETON UNIV LIBRARY; ACQUISITION SERVICE PERIODICALS on November 14, 2026 from IP address 140.180.240.0.

geometry, material system, or actuation modality, providing a general foundation for programmable multistable systems.

Materials and Methods

Origami State Machine Fabrication. Kresling (38) unit cells were fabricated by laser-cutting crease patterns (*SI Appendix*, Fig. S1) onto four paper materials with distinct mechanical properties: Taro (red cell), Copy (yellow cell), Canson (black cell), and Mixed Media (white cell). Crease patterns were folded along prescribed mountain and valley folds to form bistable unit cells. All cells share a hexagonal geometry with circumscribed radius $r = 9.8$ mm; deployed and folded heights range from 11.1 to 14.0 mm and 3.05 to 6.5 mm, respectively (*SI Appendix*, Table S1). Individual cells were assembled vertically with alternating chirality (*LH–RH–LH–RH* from bottom to top) using custom hexagonal connecting plates (0.5 mm thickness) fabricated by PolyJet 3D printing (VeroUltra White, Stratasys J55). A cylindrical NdFeB permanent magnet (grade N45; diameter 9.525 mm; thickness 3.175 mm) with in-plane magnetization ($M_0 = 1.05 \times 10^6$ A/m) was mounted at the center of the top plate to enable magnetic actuation. See more details in *SI Appendix*, section S1.

Energy Barrier Characterization. The snap-through energy barriers of individual Kresling unit cells were programmed through a combination of geometric design and material selection, yielding a well-separated ordering $\Delta U_y < \Delta U_r < \Delta U_w < \Delta U_b$ (yellow < red < white < black). Energy barriers were quantified via quasi-static torsional testing of individual unit cells. Torque–rotation responses were measured under displacement-controlled twisting with free axial translation (18), enabling extraction of characteristic quantities, including peak torque, minimum torque, and transition angles. These measurements were used both to verify the programmed energy hierarchy and to calibrate the stiffness parameters of the reduced-order dynamics model. Stiffness parameters were identified through a multiobjective goal-attainment optimization that minimizes the deviation between simulated and experimental torsional responses (19). Detailed experimental protocols, parameter identification methods, and representative mechanical characterization data are provided in *SI Appendix*, sections S1 and S5.

Magnetic Actuation System. Magnetic actuation was achieved using a custom three-axis Helmholtz coil system that generates spatially uniform magnetic fields with independently controlled magnitude and orientation (39). The system enables both pulsed fields and rotating fields for state programming and initialization, respectively. Magnetic fields were prescribed through a calibrated linear mapping between coil currents and the resulting field vector at the system center. Pulsed actuation employed in-plane fields of controlled magnitude and orientation, while rotating fields were applied at constant magnitude and frequency to induce global state convergence. Detailed system design, calibration procedures, and field characterization are provided in *SI Appendix*, section S3.

Imaging-Based Transition Tracking. State transitions were recorded using synchronized side-view and top-view imaging. The time-resolved total height and individual-cell states were extracted from the side-view image sequences, whereas the total twist-angle evolution and in-plane magnetization orientation were extracted from the synchronized top-view image sequences. Detailed imaging setup and data processing methods are provided in *SI Appendix*, section S3.

Reduced-Order Dynamics Modeling. A reduced-order Lagrangian model was developed to predict the dynamics of the multicell Kresling assembly. Each unit cell was represented by generalized coordinates for axial displacement and twist angle, with elastic responses described using a bar-and-hinge framework informed by Kresling kinematics (18). Effective stiffness parameters were identified from quasi-static torsional response data via inverse optimization, while inertial properties were determined from measured masses and geometry. Following prior studies on Kresling origami dynamics (36), energy dissipation was represented using a phenomenological linear viscous damping model, with the damping factor ν calibrated from the transition T1. Magnetic actuation was incorporated as a time-dependent torque arising from the interaction between the embedded magnet and the applied field. This formulation enables modeling of both pulsed and rotating-field actuation. Detailed model formulation, parameter identification and sensitivity analysis, and numerical implementation are provided in *SI Appendix*, sections S4 and S5.

***StateMorph* Robot Design and Fabrication.** The *StateMorph* robot is built upon the four-cell origami state machine, with additional structural elements introduced to enable controlled locomotion and reconfiguration under global magnetic actuation. Two hexagonal end caps were fabricated using PolyJet 3D printing (VeroUltra Clear, Stratasys J55) and attached to the two ends of the assembly. Both end caps have a circumscribed radius of 13 mm, but differ in edge thickness (3 and 1 mm), resulting in asymmetric frictional interactions with the substrate. The thicker end (3 mm) corresponds to a high-friction interface (μ_{high}), while the thinner end (1 mm) provides a low-friction interface (μ_{low}). During state transitions, this asymmetry enables selective cell switching, with the high-friction end anchoring the structure and the low-friction end enabling reconfiguration and displacement. Permanent magnets with in-plane magnetization were embedded within both end caps. In the fully deployed configuration, the magnetization directions of the two magnets differ by approximately 140°, enabling asymmetric torque generation under a uniform magnetic field and facilitating controlled actuation. To investigate locomotion under confinement, a stepped channel was fabricated using the same transparent material. The channel consists of three segments with lengths of 60 mm and widths of 66 mm, 54 mm, and 66 mm, respectively. The bottom surface was covered with Canson paper to provide a uniform friction substrate.

Data, Materials, and Software Availability. The experimental data and the simulation software supporting the findings of this study are openly available at Zenodo (40). The physical materials used in this study have been elaborated in detail in Materials and Methods.

ACKNOWLEDGMENTS. We thank S. Zang for sharing MATLAB code for reference on the geometric and energy calculations of the Kresling unit cell, and for providing comments and suggestions on the figures. Y.R. acknowledges financial support from the Distinguished Postdoctoral Fellowship Program at the Andlinger Center for Energy and the Environment, Princeton University. We also acknowledge support from the "Princeton Catalysis Initiative" at Princeton University, and the NSF under Grants Nos. 2323276 and 2414295. Any opinions, findings, and conclusions or recommendations expressed in this material are those of the authors and do not necessarily reflect the views of the sponsors.

Author affiliations: [a]Andlinger Center for Energy and the Environment, Princeton University, Princeton, NJ 08544; [b]Department of Electrical and Computer Engineering, Princeton University, Princeton, NJ 08544; [c]Department of Civil and Environmental Engineering, Princeton University, Princeton, NJ 08544; and [d]Princeton Materials Institute, Princeton University, Princeton, NJ 08544

1. Y. Li, S. Pellegrino, A theory for the design of multi-stable morphing structures. *J. Mech. Phys. Solids* **136**, 103772 (2020).
2. T. Chen, M. Pauly, P. M. Reis, A reprogrammable mechanical metamaterial with stable memory. *Nature* **589**, 386–390 (2021).
3. H. Yasuda *et al*., Mechanical computing. *Nature* **598**, 39–48 (2021).
4. Z. Meng *et al*., Encoding and storage of information in mechanical metamaterials. *Adv. Sci.* **10**, 2301581 (2023).
5. T. Mei, C. Q. Chen, In-memory mechanical computing. *Nat. Commun.* **14**, 5204 (2023).
6. P. Jiao, J. Mueller, J. R. Raney, X. Zheng, A. H. Alavi, Mechanical metamaterials and beyond. *Nat. Commun.* **14**, 6004 (2023).
7. Y. Li *et al*., Reprogrammable and reconfigurable mechanical computing metastructures with stable and high-density memory. *Sci. Adv.* **10**, eado6476 (2024).
8. J. Byun, A. Pal, J. Ko, M. Sitti, Integrated mechanical computing for autonomous soft machines. *Nat. Commun.* **15**, 2933 (2024).

Downloaded from https://www.pnas.org by PRINCETON UNIV LIBRARY; ACQUISITION SERVICE PERIODICALS on November 14, 2026 from IP address 140.180.240.0.

9. W. Chen *et al*., Scalable jet swimmer driven by pulsatile artificial muscles and soft chamber buckling. *Adv. Mater.* **37**, 2503777 (2025).
10. D. Misseroni *et al*., Origami engineering. *Nat. Rev. Methods Primers* **4**, 40 (2024).
11. J. L. Silverberg *et al*., Using origami design principles to fold reprogrammable mechanical metamaterials. *Science* **345**, 647–650 (2014).
12. W. Yan *et al*., Origami-based integration of robots that sense, decide, and respond. *Nat. Commun.* **14**, 1553 (2023).
13. C. Lv, D. Krishnaraju, G. Konjevod, H. Yu, H. Jiang, Origami based mechanical metamaterials. *Sci. Rep.* **4**, 5979 (2014).
14. X. Hu, T. Tan, B. Wang, Z. Yan, A reprogrammable mechanical metamaterial with origami functional-group transformation and ring reconfiguration. *Nat. Commun.* **14**, 6709 (2023).
15. H. Yasuda, T. Tachi, M. Lee, J. Yang, Origami-based tunable truss structures for non-volatile mechanical memory operation. *Nat. Commun.* **8**, 962 (2017).
16. Z. Zhai, Y. Wang, H. Jiang, Origami-inspired, on-demand deployable and collapsible mechanical metamaterials with tunable stiffness. *Proc. Natl. Acad. Sci. U.S.A.* **115**, 2032–2037 (2018).
17. B. Tan *et al*., Bistable origami thermal switch with high switching ratios. *Nat. Commun.* **17**, 3177 (2026).
18. S. Zang, D. Misseroni, T. Zhao, G. H. Paulino, Kresling origami mechanics explained: Experiments and theory. *J. Mech. Phys. Solids* **188**, 105630 (2024).
19. T. Zhao *et al*., Modular chiral origami metamaterials. *Nature* **640**, 931–940 (2025).
20. K. Liu, T. Tachi, G. H. Paulino, Invariant and smooth limit of discrete geometry folded from bistable origami leading to multistable metasurfaces. *Nat. Commun.* **10**, 4238 (2019).
21. J. Liu *et al*., Controlled pathways and sequential information processing in serially coupled mechanical hysterons. *Proc. Natl. Acad. Sci. U.S.A.* **121**, e2308414121 (2024).
22. L. J. Kwakernaak, M. van Hecke, Counting and sequential information processing in mechanical metamaterials. *Phys. Rev. Lett.* **130**, 268204 (2023).
23. C. Coulais, A. Sabbadini, F. Vink, M. van Hecke, Multi-step self-guided pathways for shape-changing metamaterials. *Nature* **561**, 512–515 (2018).
24. S. Zang, T. Zhao, D. Misseroni, G. H. Paulino, Origami frustration and its influence on energy landscapes of origami assemblies. *Proc. Natl. Acad. Sci. U.S.A.* **122**, e2426790122 (2025).
25. D. Melancon, A. E. Forte, L. M. Kamp, B. Gorissen, K. Bertoldi, Inflatable origami: Multimodal deformation via multistability. *Adv. Funct. Mater.* **32**, 2201891 (2022).
26. C. Zhang *et al*., Plug & play origami modules with all-purpose deformation modes. *Nat. Commun.* **14**, 4329 (2023).
27. S. Wu, T. Zhao, Y. Zhu, G. H. Paulino, Modular multi-degree-of-freedom soft origami robots with reprogrammable electrothermal actuation. *Proc. Natl. Acad. Sci. U.S.A.* **121**, e2322625121 (2024).
28. C. Chen *et al*., Advancing physical intelligence for autonomous soft robots. *Sci. Rob.* **10**, eads1292 (2025).
29. D. C. Bershadsky, T. Zhao, G. H. Paulino, E. C. Davidson, Digital actuation control of soft robotic origami with self-folding liquid crystal elastomer hinges. *Adv. Funct. Mater.*, e25150 (2026).
30. Y. Kim, H. Yuk, R. Zhao, S. A. Chester, X. Zhao, Printing ferromagnetic domains for untethered fast-transforming soft materials. *Nature* **558**, 274–279 (2018).
31. Y. Kim, X. Zhao, Magnetic soft materials and robots. *Chem. Rev.* **122**, 5317–5364 (2022).
32. D. Tang *et al*., Bistable soft jumper capable of fast response and high takeoff velocity. *Sci. Rob.* **9**, eadm8484 (2024).
33. L. S. Novelino, Q. Ze, S. Wu, G. H. Paulino, R. Zhao, Untethered control of functional origami microrobots with distributed actuation. *Proc. Natl. Acad. Sci. U.S.A.* **117**, 24096–24101 (2020).
34. Y. Luo *et al*., Intrinsically multistable soft actuator driven by mixed-mode snap-through instabilities. *Adv. Sci.* **11**, 2307391 (2024).
35. H. Yasuda *et al*., Data-driven prediction and analysis of chaotic origami dynamics. *Commun. Phys.* **3**, 168 (2020).
36. H. Yasuda *et al*., Origami-based impact mitigation via rarefaction solitary wave creation. *Sci. Adv.* **5**, eaau2835 (2019).
37. R. Pappu, B. Recht, J. Taylor, N. Gershenfeld, Physical one-way functions. *Science* **297**, 2026–2030 (2002).
38. B. Kresling, "Natural twist buckling in shells: From the Hawkmoth's bellows to the deployable Kresling-pattern and cylindrical Miura-ori (2008)" *Proceedings of the 6th International Conference on Computation of Shell and Spatial Structures IASS-IACM: "Spanning Nano to Mega"*, J. F. Abel, J. R. Cooke, Eds. (Cornell University, Ithaca, NY, 2008), pp. 18–21.
39. K. Manos *et al*., "Wireless actuation of magnetic robots with a modular 60 mt 3-D Helmholtz coil system" in *2025 IEEE Applied Power Electronics Conference and Exposition (APEC)* (IEEE, 2025), pp. 1274–1278.
40. Y. Rao, K. Manos, T. Zhao, M. Chen, G. H. Paulino, Origami state machine with time-varying magnetic fields [Computer software]. Zenodo. https://doi.org/10.5281/zenodo.23288257. Deposited 12 October 2026.

Downloaded from https://www.pnas.org by PRINCETON UNIV LIBRARY; ACQUISITION SERVICE PERIODICALS on November 14, 2026 from IP address 140.180.240.0.